IOP Publishing

Journal of Micromechanics and Microengineering

J. Micromech. Microeng. **28** (2018) 105010 (10pp)

https://doi.org/10.1088/1361-6439/aacf35

A bi-stable vertical magnetic actuator with non-contact latching based on magnetic microlamination technology

Yuan Li, Minsoo Kim and Mark G Allen

Department of Electrical and Systems Engineering, University of Pennsylvania, Philadelphia, PA 19104, United States of America

E-mail: yuanli1@seas.upenn.edu

Received 10 April 2018, revised 29 May 2018
Accepted for publication 26 June 2018
Published 11 July 2018

Abstract

We present the design, fabrication and testing of a bi-stable vertical magnetic actuator which exhibits non-contact latching behavior that is enabled by magnetic microlamination technology. The lamination technology translates the structural periodicity (i.e. the multilayers of alternating magnetic and nonmagnetic materials) into magnetic-field-pattern periodicity, which in turn results in multi-stable energy states of the microsystem and leads to the defined latching behavior. A single-mask process is utilized to reduce the fabrication complexity of this actuator. The actuator has bi-stable vertical latching positions 40 μm-apart and the latching mechanism is solely based on magnetostatic interaction without the need for a mechanical stop. Input energies as low as 0.6 mJ for switching up and 0.02 mJ for switching down are needed to fulfill one full period of the bi-stable actuation. No external energy is needed in the latching positions. The behavior of the actuator is explained in terms of the energy landscape theory. These types of vertical multi-stable actuators could have potential applications as valves in micro-fluidic controls, or as integral parts of micro-mirrors in optical applications.

Keywords: bi-stable, magnetic actuator, multilayer, single-mask process, latching, microelectromechanical systems

S Supplementary material for this article is available online

(Some figures may appear in colour only in the online journal)

1. Introduction

Microelectromechanical systems (MEMS)-based actuators are a key research area, with a wide range of applications including valves [1], stepper motors [2], and relays [3]. Electrostatic actuators are by far the most popular type of MEMS actuators, but can suffer from high actuating voltage, short actuating range and/or low actuation force [4]. Magnetic MEMS actuators can alleviate some of these issues; however, integrating exotic magnetic materials in a CMOS-compatible and fully integrated manner, and/or fabricating dense coils, typically requires much more intensive microfabrication effort than their electrostatic counterparts. These complexities have hindered the technological progress of these small-scale magnetic actuators [5].

Latching schemes for actuators are often desirable since they allow actuators to remain in defined states with no expenditure of energy. Typical approaches to magnetic actuator latching have involved a combination of electromagnetic actuation with electrostatic latching [6], or the use of a mechanical stop [1]. While effective latching can be realized using these approaches, there are other operation scenarios where non-contact latching (i.e. positional latching without touching a mechanical stop) is desirable.

Among the various actuation mechanisms for magnetic MEMS systems, two types are most commonly seen [7]: in one type, actuation is induced due to the minimization of magnetic reluctance (e.g. closing of a magnetic circuit); in the other, actuation arises as Lorentz force acts on a current carrying wire. These two mechanisms can be invoked individually to realize the desired actuation, or they can be combined to achieve both actuation and latching, in an effort to reduce energy consumption. An excellent example of this hybrid mechanism can be found in [8], where actuation is achieved utilizing the combined effects of Lorentz force (current to magnet) and minimization of magnetic reluctance (magnet to magnet), while latching is achieved by harnessing the magnetostatic force from the closing of a magnetic circuit, together with a mechanical stop. This process requires multiple alignment steps and a wafer bonding process, due to the latching and actuation mechanisms used.

In this work, we propose a bi-stable vertical magnetic actuator design that utilizes only magneto-static force to realize latching (without any mechanical contact), and by integrating a current conductor and a permeable component into a single piece, we significantly reduce the fabrication complexity down to a single-mask process. This single-mask process is enabled by two recently-developed technologies: a single-mask process for dual-height metallic structures [9]; and a robotic-assisted magnetic lamination technology [10, 11]. The magnetic lamination technology in which permeable and non-permeable materials are sequentially electrodeposited in a multilayer fashion has been previously used to achieve multilayer surface/interface-property enabled functions and applications (e.g. microlaminated MEMS magnets with preserved magnetic properties [12]), and multilayer bulk-property enabled functions and applications (e.g. nanolaminated inductor cores with suppressed eddy-current losses [13]). In this work, both the architectural sequence and the periodic magnetic field patterns of the magnetic multilayer are exploited to create a bi-stable microsystem that enables defined latching behaviors.

2. Actuator design

2.1. Operation principle

The operation principle of the bi-stable vertical magnetic actuator is shown in cross-sectional view in figure 1. For ease of understanding, consider a simplified latching mechanism shown in figure 1(a). A movable, magnetically permeable, electrically conducting piece is flanked by two fixed permeable pieces (with narrow gaps between the movable and the fixed pieces), and placed in an external magnetic field oriented in the horizontal direction (refer to figure 1). If only one degree of freedom of motion is available, namely the vertical direction ($\pm y$ direction), the movable piece has a tendency to align with the pair of fixed pieces to reduce magnetic potential energy. This serial configuration corresponds to the energy minimal state in an energy well, hence the stable position. If two pairs instead of one pair of fixed permeable pieces are stacked in the vertical direction separated by a layer of a non-permeable (of much lower relative permeability (e.g. unity) material, similarly, two energy minimal states are created, one position (latching-down (LD) state, figure 1(b)) nearly aligned with the bottom and the other (latching-up (LU) state, figure 1(e)) nearly aligned with the top pair of the fixed permeable pieces. Note that the near-alignment, rather than perfect-alignment, is due to the interactions of the movable piece with both the top and bottom pairs of the fixed permeable pieces. The transition between one energy minimum to the other requires external energy input. Applying a current pulse through the movable permeable piece (i.e. also using it as a conductible piece) in the presence of the external magnetic field results in a Lorentz force which can be exploited to switch the movable piece between LU and LD states. Assuming the movable piece is initially in the LD state (figure 1(b)), a proper pulsed current (directed into the plane of the figure along with a left-pointing external field) would break the latching and initiate an upward movement (pulsing-up (PU) state, figure 1(c)). If sufficient current to overcome the energy barrier, i.e. the UPFB, has been applied, the upward movement continues without additional current input due to inertia until it surpasses the energy barrier (unstable-equilibrium (UE) state, figure 1(d)), after which it falls into the other energy well, i.e. the LU state (figure 1(e)). Similarly, a current that is induced in the opposite direction would initiate the pulsing-down (PD) state (figure 1(f)). The actuator will fall into the LD state if the current is sufficiently large to overcome the corresponding DPFB.

Should the stacking of the vertical fixed pairs of permeable pieces be continued, additional energy wells can be created, forming a multi-stable system that can pave the way for applications such as vertical stepper motors with defined stepping sizes. In this work, we focus on the bi-stable system with two pairs of fixed permeable pieces.

The designed 3D bi-stable actuator design is shown in figure 2. Three main components are presented: (1) a pair of tri-layer 'flux guides' which are the fixed permeable/non-permeable/permeable stacks in figure 1; (2) a single-layer, serpentine-shaped 'shuttle' which is the vertically movable permeable piece in figure 1; and (3) a pair of contact pads which operate as mechanical anchors and electrical contacts. Note that the serpentine spring is designed to act both as a current path for the Lorentz switching force, as well as to provide a mechanical support for the vertical movement of the shuttle.

2.2. Material selection

The device is fabricated on a glass substrate. Glass is utilized for its electrical insulation as well as optical transparency to facilitate the fabrication process. Permalloy ($Ni_{80}Fe_{20}$) is used as the permeable material due to its high permeability ($\mu_r = 900$), saturation flux density ($B_s = 1.2$ T) and process compatibility. The material properties of electrodeposited Permalloy can be find in [13]. Copper is used as the non-permeable material due to its high electrical conductivity, which facilitates subsequent electrodeposition.

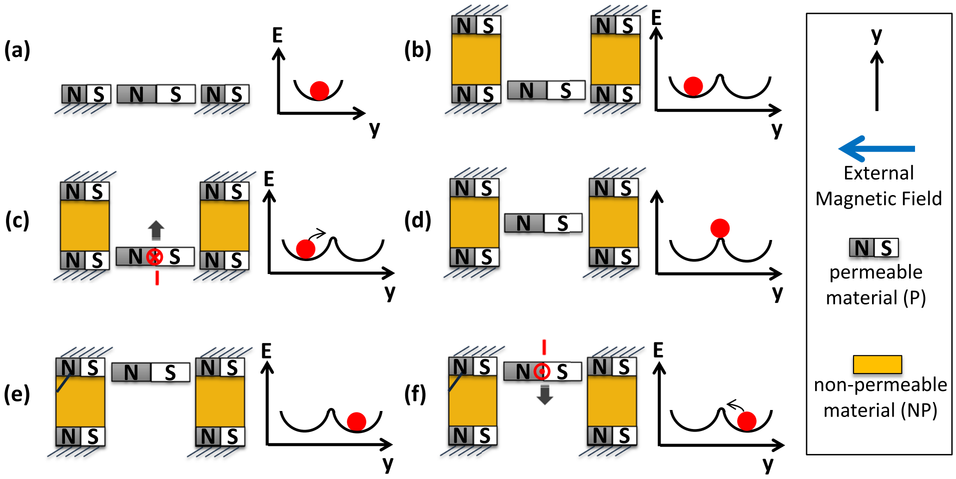

Figure 1. Operating principle of the bi-stable magnetic actuator (cross-sectional view). (a) A movable permeable piece has a tendency to latch in alignment with a pair of fixed permeable pieces to reduce magnetic potential energy, so to stay in an energy well. Two pairs of fixed permeable pieces stacked in the vertical direction separated by non-permeable pieces, and the movable permeable piece latched at the latching-down (LD) state (b); at the pulsing-up (PU) state (c) initiating upward motion due to Lorentz Force produced by a pulse of current; at the unstable equilibrium (UE) state (d) barely going over the energy barrier; latched at the latching-up (LU) state (e); and at the pulsing-down (PD) state (f) initiating downward motion due to Lorentz force produced by an opposite pulse of current.

2.3. Device modeling

The proposed actuation and latching mechanism involves three forces: (1) magneto-static force; (2) spring force; and (3) Lorentz force. Since bi-stable latching is enabled only when these forces are balanced appropriately, a comprehensive analysis of these forces is very important. All three forces exist during the pulsing-up and -down states (figures 1(c) and (f)). At all other states (including LD (figure 1(b)), LU (figure 1(e)), unstable equilibrium states (figure 1(d)), and anywhere in-between, only magneto-static and spring forces are present.

First, we model the magnetostatic force exerted on the shuttle, to design a proper gap in between the shuttle and the flux guides. When the gap is sufficiently small, the actuator will possess two stable latching states, LU and LD. Second, a spring is designed such that the mechanical restoring force of the spring is sufficiently small so as to not overwhelm the magnetostatic latching forces. Third, the LU and LD positions, where the total passive force (i.e. superposition of the magnetostatic and spring forces) acting on the shuttle becomes zero, are determined. The upward-passive-force-barrier (UPFB) and downward-passive-force-barrier (DPFB), i.e. the forces that must be overcome to switch the shuttle from one latching position to the other, are calculated. Lastly, the necessary minimum input currents to switch between LU and LD positions are estimated by balancing the calculated passive-force-barriers with the Lorentz force.

A vertical actuator is designed such that (1) a reliable bi-stable latching is achieved while (2) the necessary input current pulses are sufficiently small to be supplied by a typical DC current source (e.g. <0.5 A); this device is referred to as type A device. As a control, a type B device without latching capability is designed.

2.3.1. Magnetostatic force. The origin of magnetostatic latching force is the magnetic interaction between a Permalloy shuttle and flux guides. The device geometry and the coordinate system are shown in figure 3(a). The x- and z- components of the magnetostatic force are assumed to be zero since the device is symmetric with respect to the y axis. The y-component of the magnetostatic force ($F_{M,y}$) experienced by the shuttle could be analytically calculated using Kelvin's formula as shown in equation (1) [1, 14]:

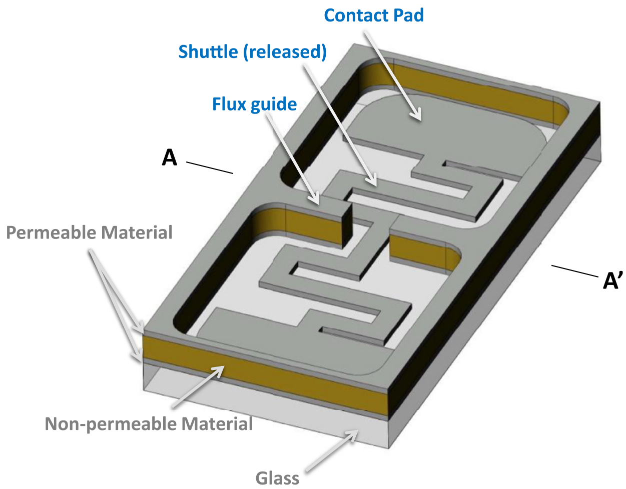

Figure 2. 3D design sketch of the bi-stable vertical magnetic actuator. Tri-layer (permeable/non-permeable/permeable) flux guide, shuttle and contact pad as marked. A-A′ indicating the cross-sectional cut demonstrated in figure 5.

$$F_{M,y} = VM_x \frac{dB_x}{dy} \quad (1)$$

where V and M_x are the volume and x-component magnetization of the shuttle, respectively, and B_x is the x-component of the magnetic flux density *without* the presence of the shuttle. As observed in equation (1), the force $F_{M,y}$ is proportional to dB_x/dy.

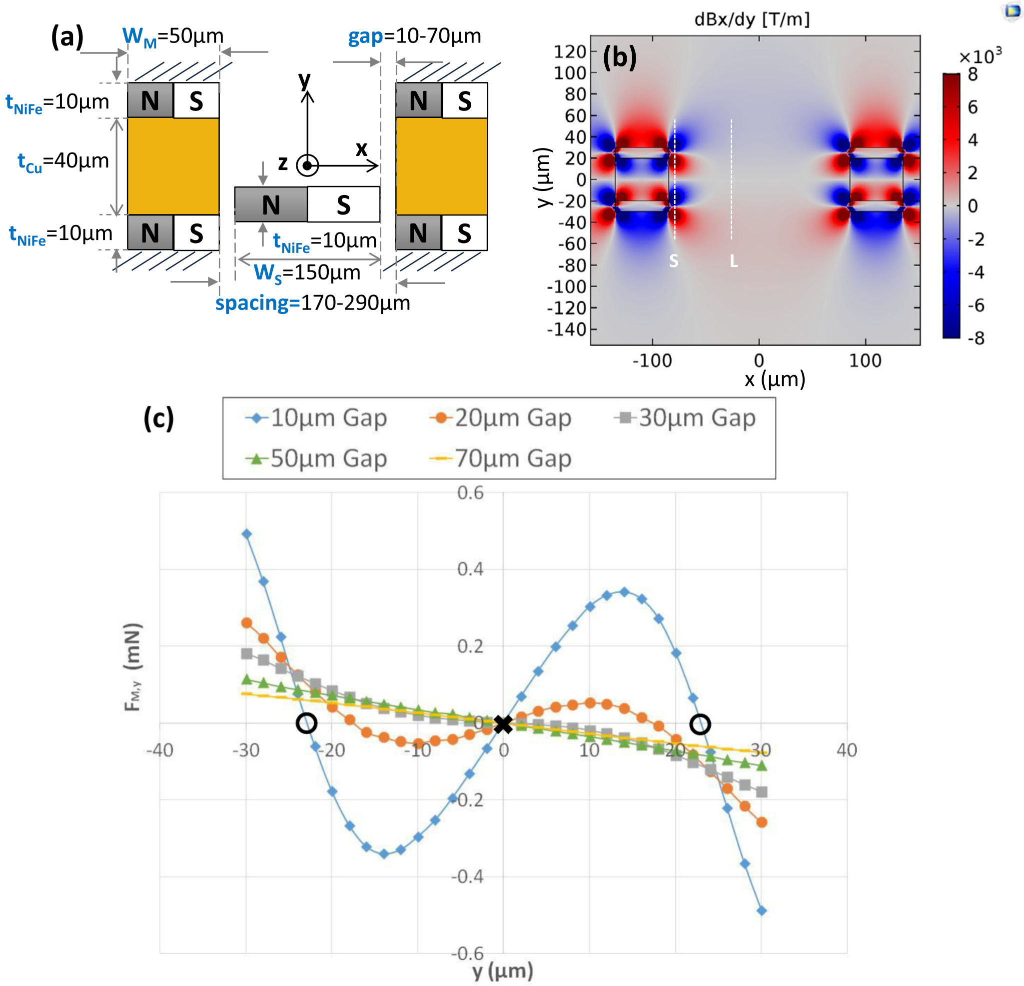

Figure 3. (a) Schematic showing the proper coordinate system and dimensions. Note the term 'spacing' is utilized to indicate the distance between two flux guides, while the term 'gap' is utilized to indicate the distance between the edge of the shuttle and the flux guides. (b) A 2D map of simulated dB_x/dy, when the spacing equals 170 μm, and no shuttle is present within the flux guides. The dotted lines show the relative proximity of the shuttle edge (when presented) to the flux guides, with small gaps (edge at S line) and large gaps (edge at L line). (c) Simulated magneto-static latching force ($F_{M,y}$) versus vertical displacement of the bi-stable magnetic actuator using finite-element analysis for gap sizes 10, 20, 30, 50, and 70 μm. A force sign convention is used such that a force along the positive y direction is deemed positive. Uniform external magnetic flux density of B_0 (0.75 T) is applied in the models.

The flux gradient dB_x/dy is calculated, without the presence of a shuttle, using 2D finite-element analysis (FEA) (figures 3(a) and (b)); the 2D magnetostatic simulations are performed based on COMSOL Multiphysics AC/DC module. The magnetostatic force that will be potentially induced to a shuttle could be estimated by tracking the magnitude and the sign of dB_x/dy along the vertical imaginary traces that are positioned between the flux guides; these traces will correspond to the moving edge of the shuttle. It can be observed that the shuttle will actuate in two different modes depending on its relative proximity to the flux guides. For example, consider the shuttle moving along the trace 'S', which is close to the flux guides. The sign of dB_x/dy changes three times; hence, the magnetostatic force (exerted to the shuttle) would also exhibit three sign changes. Such an actuator would exhibit bi-stable latching, as will be discussed shortly. On the contrary, the shuttle moving along the trace 'L' will be subjected to a force which sign changes only once; such actuator will be in the non-latching mode.

These two potential actuation modes are confirmed by simulating the magnetostatic force imposed to a shuttle as a function of vertical position (or, as a function of y), parameterized by the gap between the shuttle and the flux guide (i.e. 10, 20, 30, 50 and 70 μm) using FEA (figure 3(c)). A force sign convention is used such that a force in the positive y direction is deemed positive. Two types of devices (i.e. type A device with 10 μm gap and type B device with 50 μm gap) are considered; as mentioned earlier, the former represents a bi-stable latching device, while the latter represents a non-latching device. Type A device exhibits LD and LU positions indicated by the black circles, where magnetostatic forces are equal to zero in addition to negative slopes indicating high stability (i.e. negative force is incurred when the shuttle is trying to move in the positive direction, and vice versa). The origin of these high stability positions is the relatively large change of dB_x/dy in close proximity to the flux guides. The black X marks the state of UE between them (positive displacement

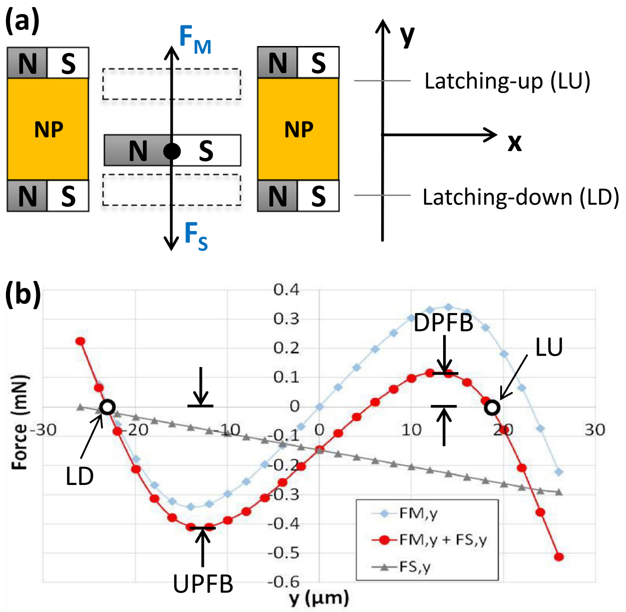

Figure 4. (a) Schematics of the passive force (sum of magnetostatic force ($F_{M,y}$) and spring force ($F_{S,y}$)) and stable latching positions (LD and LU) of the bi-stable actuator. (b) Simulated passive force ($F_{M,y} + F_{S,y}$) versus vertical displacement of type A device, from which LD, LU, upward-passive-force-barrier (UPFB) and downward-passive-force-barrier (DPFB) could be determined. A force sign convention is used such that a force along the positive y direction is deemed positive.

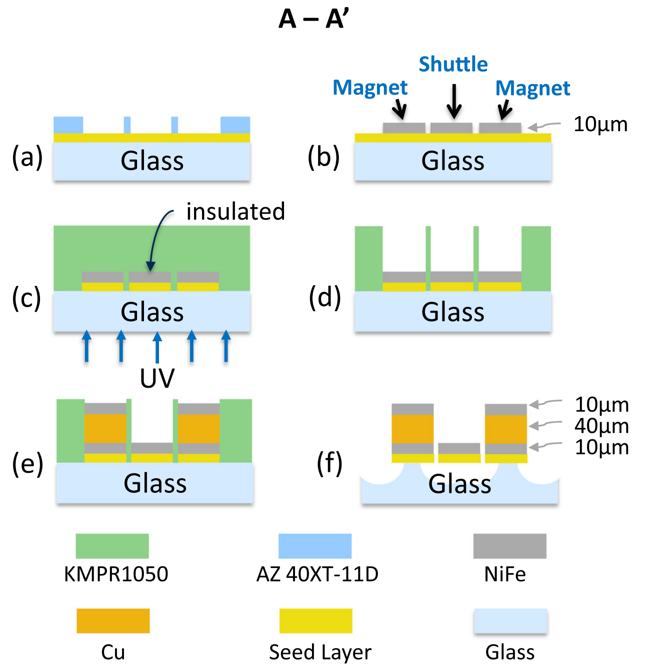

Figure 5. Fabrication sequence (side view, cross-section A-A′ of figure 2) of the bi-stable actuator using a single mask. (a) Sputtering of Ti/Cu/Ti seed layer on glass substrate and patterning positive resist mold; (b) electrodeposition of NiFe layer followed by positive resist mold stripping; (c) exposed seed layer wet-etching, electrically insulating the shuttle region followed by negative resist spinning and backside UV exposure; (d) negative resist development, forming a self-aligned mold; (e) electrodeposition of Cu and NiFe sequentially on the flux guide region only; and (f) negative resist mold stripping followed by glass substrate wet-etching, releasing the shuttle from the substrate.

incurs positive-signed force causing further displacement, and vice versa). On the contrary, the magnetostatic force that is induced to type B device shows a monotonic variation along with vertical displacement; no stable latching positions are observed.

In summary, to operate an actuator in the latching mode, and thereby achieve bi-stable actuation, the designed shuttle-to-flux-guide gap should be sufficiently small (<20 μm, in this specific case). Note this is true only if t_{Cu} is sufficiently large to magnetically decouple the top and bottom permeable layers of the flux guides.

2.3.2. Spring force. A properly designed spring must (1) exhibit sufficiently low vertical spring constant to not overwhelm the magnetostatic latching force; and (2) possessing sufficiently high lateral spring constant to minimize spurious lateral ($\pm x$-direction) actuation; a long, thin serpentine spring with a sufficiently large spring width (150 μm) is designed accordingly.

The mechanical restoration force of the spring (i.e. or simply, the spring force ($F_{S,y}$)) is simulated as a function of vertical displacement using finite element analysis (COMSOL MEMS module) and the result is plotted in figure 4(b) (Spring constant: 5.7 N m^{-1}). The asymmetrical spring force results from the fabrication-influenced design of the zero spring deflection position aligned with the bottom pair of the permeable pieces (i.e. directly on top of the substrate) instead of the center of the flux guides.

2.3.3. Passive force. The total passive force is calculated as the superposition of magnetostatic force and spring force, i.e. $F_{M,y} + F_{S,y}$. The passive force is calculated for type A device (i.e. the devices with 10 μm gap). The latching positions (LD and LU, figure 4(a)) are determined at which the actuator experiences zero passive force. The calculated LD (also PU) and LU (also PD) positions of type A device are determined to be -23.1 μm and 18.4 μm, respectively (figure 4(b)). Hence, the designed actuation range would be 41.5 μm. The upward-passive-force-barrier (UPFB $= -0.409$ mN) and downward-passive-force-barrier (DPFB $= 0.116$ mN) are calculated from figure 4(b); the difference between UPFB and DPFB is due to the asymmetric spring force.

2.3.4. Lorentz force.

$$\overrightarrow{F_{L,\,PU}} = \int \vec{I} \times \overrightarrow{B_x(x, y_{PU}, z)}\, dl = I_{PU,z}\left[\overline{B_x\,(y_{PU})}L_{FG} + B_0 L_R\right]\hat{y} = F_{L,PU,y}\hat{y} \quad (2)$$

$$\overrightarrow{F_{L,\,PD}} = \int \vec{I} \times \overrightarrow{B_x(x, y_{PD}, z)}\, dl = I_{PD,z}\left[\overline{B_x\,(y_{PD})}L_{FG} + B_0 L_R\right]\hat{y} = F_{L,PD,y}\hat{y} \quad (3)$$

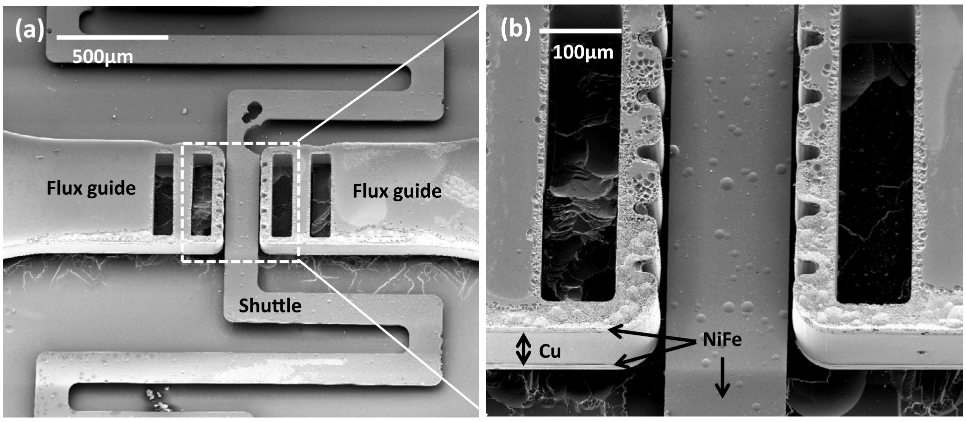

Figure 6. SEM micrographs of the bi-stable actuator type A (a) and its enlarged view (b). The fully released single-layer NiFe shuttle with a thickness of 10 μm is flanked by two tri-layer (NiFe 10 μm/Cu 40 μm/NiFe 10 μm) flux guides (flux guides undercutted but not fully released). Gaps in between shuttle and flux guide is 10 μm wide.

$$\text{where } \overline{B_x\left(y_{PU}\right)} = \frac{1}{W_s}\int_{-\frac{1}{2}W_s}^{\frac{1}{2}W_s} B_x\left(x, y_{PU}\right)dx \tag{4}$$

$$\overline{B_x\left(y_{PD}\right)} = \frac{1}{W_s}\int_{-\frac{1}{2}W_s}^{\frac{1}{2}W_s} B_x\left(x, y_{PD}\right)dx. \tag{5}$$

The Lorentz force can be estimated using equations (2)–(5), assuming (1) uniform current distribution; (2) constant $B_x(x,y,z)$ over the thickness (y direction extent) of the thin shuttle; and (3) negligible fringing effects. In equations (2) and (3), the Lorentz force at PU and PD states, respectively (i.e. $\overrightarrow{F_{L,\ PU}}$ and $\overrightarrow{F_{L,\ PD}}$), are the functions of the x-component of the magnetic flux densities at PU and PD, respectively (i.e. $\overrightarrow{B_x\left(x, y_{PU}, z\right)}$ and $\overrightarrow{B_x\left(x, y_{PD}, z\right)}$). The calculation of Lorentz force can be simplified by using the average x-component of flux densities between the flux guides at PU and PD positions (i.e. $\overline{B_x\left(y_{PU}\right)}$ and $\overline{B_x\left(y_{PD}\right)}$, in equations (4) and (5)). Note these fluxes are calculated without the shuttle being involved [15, 16]. The simulated (COMSOL, AC/DC module) average fluxes are $\overline{B_x\left(y_{PU}\right)}$ =0.789 T and $\overline{B_x\left(y_{PD}\right)}$ = 0.788 T, respectively. The parameter L_{FG} (0.5 mm) is the designed length of the shuttle between flux guides in the z direction, L_R (2.3 mm) is the designed total shuttle length in the z direction that is perpendicular to the ambient field, and W_s (150 μm) is the designed width of the shuttle. The calculation of the necessary $I_{PU,z}$ and $I_{PD,z}$, i.e. the necessary current to switch between LU and LD states, follows. Here, a current sign convention is used such that a current into the plane (figures 3 and 4) is treated as a positive current. With the external magnetic field induced toward the negative x direction, a positive current generates a positive Lorentz force to the positive y direction.

2.3.5. Lorentz force versus passive force. The Lorentz force should exceed the passive-force-barrier (i.e. $F_{L,PU,y} >$ UPFB and $F_{L,PD,y} >$ DPFB), to actuate a shuttle from one latching state to the other. Using equations (2)–(5), along with the calculated UPFB and DPFB (figure 4(b)), the necessary pulsing-up and -down current of 0.19 A and −0.05 A, respectively, are calculated.

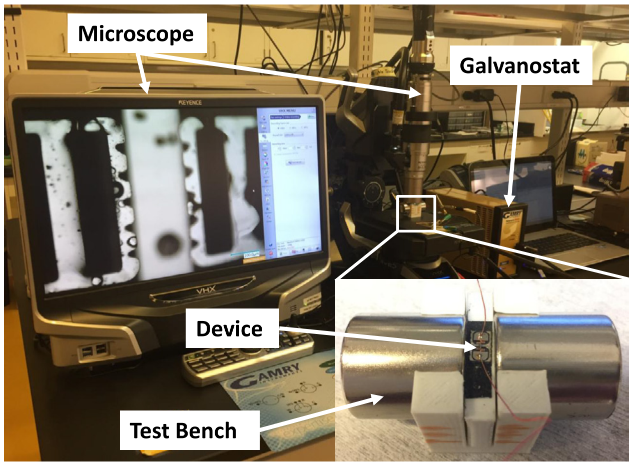

Figure 7. Experimental setup for the characterization of the bi-stable vertical magnetic actuator, including a digital microscope, a test bench and a galvanostat.

3. Fabrication sequence

The fabrication sequence must contemplate the realization of two essential features for actuator operation: dual-height structures, i.e. structures in which the shuttle is single-layered in contrast with nearby tri-layered flux guides; and the ability to separate the dual height structures by narrow gaps for proper bi-stable latching. Conventional multimask layer-by-layer fabrication is not ideal for the proposed design, due to increased fabrication complexity and alignment issues associated with thick, multiheight structures [17]. Hence, we developed a fabrication process capable of creating dual-height magnetic structures separated by a narrow gap detailed in [9]. A brief process description is provided here for the convenience of the reader, as shown in figure 5.

A glass wafer was used as a substrate, and a titanium(30 nm)/copper(300 nm)/titanium(30 nm) seed layer was sputtered onto the substrate. An AZ40XT photoresist mold was formed

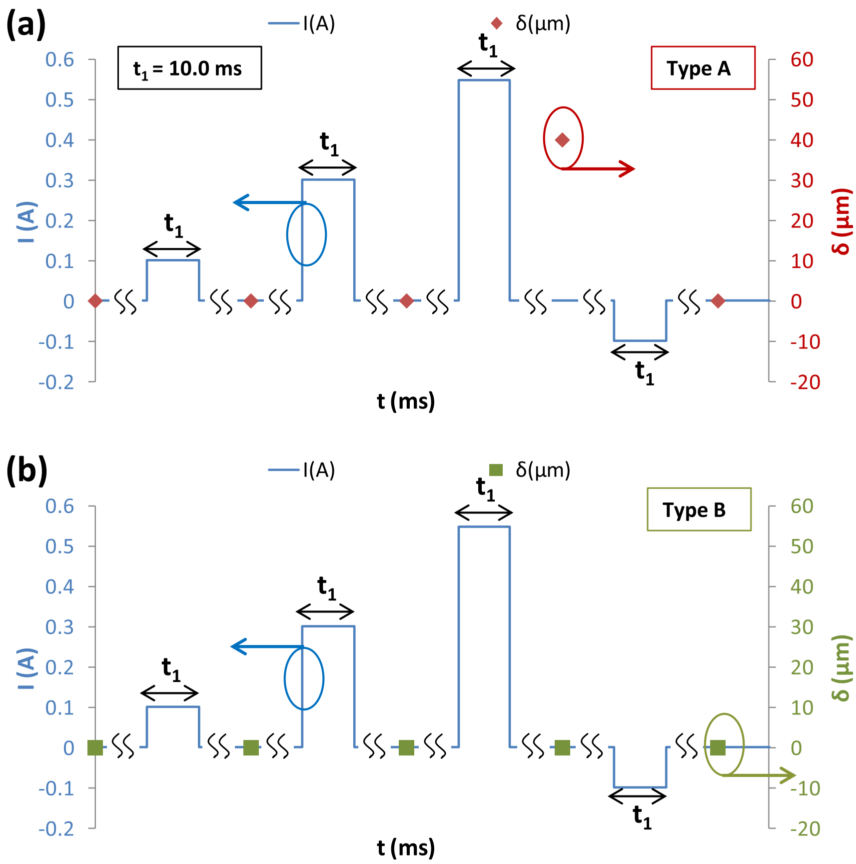

Figure 8. Static vertical displacement measured using digital microscope with a fixed pulse duration (t_1 of 10.0 ms) and various actuating current pulses (0.1, 0.3, and 0.55 A in pulse height) for (a) type A device (10 μm gap), showing an LU state 40 μm from the LD state could be triggered with a 0.55 A pulse, followed by a return of the LD state with a reverse pulse of −0.1 A. (b) Type B device (50 μm-gap), showing no LU state regardless of the pulse heights.

on the seed layer (figure 5(a)) and conventional through-mold electrodeposition of a 10 μm $Ni_{80}Fe_{20}$ Permalloy layer was subsequently carried out to form the entirety of the shuttle and the bottom layer of the flux guides. After removing the AZ40XT mold (figure 5(b)), using the deposited NiFe as an etch-mask, the titanium/copper/titanium seed layer was wet-etched. Upon completion of this step, the shuttle and contact pad region formed an inner region electrically insulated from the outer regions. The area between these regions became transparent due to the removal of the seed layer exposing the underlying glass substrate. A thick KMPR1050 photoresist was then spun on the wafer and, utilizing the electroformed Permalloy as a lithography mask, UV exposure from the backside of the wafer (figure 5(c)) followed by development created a high-aspect-ratio (HAR, 10:1) photoresist mold for a second round of electrodeposition (figure 5(d)). The second round of electrodeposition [13] comprised a 40 μm Cu layer and a 10 μm NiFe layer to form the remaining layers of the flux guides (figure 5(e)). Since the shuttle is not electrically connected to the flux guide areas, no electrodeposition occurs in the shuttle region. After dissolving the KMPR resist mold, the wafer was subsequently immersed in hydrofluoric acid solution (commercial (KMG) buffered oxide etchant (BOE), 6:1 volume ratio of 40% NH_4F in DI water to 49% HF) to undercut the glass substrate and release the shuttle (figure 5(f)). The wafer was then diced using a green laser (IPG IX280-DXF). Two types of devices are fabricated, type A and type B. The SEM micrographs of a type A featuring the BOE released Permalloy shuttle is shown in figure 6(a) with an expanded view in figure 6(b). Some etching defects (e.g. pinholes and surface roughness) are visible in the SEM images. Ideally, hydrofluoric acid and BOE should have good selectivity to Permalloy [18] and Copper [19], and the usage of BOE to release Permalloy structures from silicon dioxide substrates has been demonstrated [18]. However, Nickel oxide and Copper oxide can be attacked by hydrofluoric solutions [20, 21], which might be a possible cause for the etching defects on the actuator structure.

4. Device characterization

Characterization of the fabricated devices (type A and B) was performed as shown in figure 7. An external magnetic field of 0.75 T was provided through a pair of NdFeB permanent magnets (K&J magnetics, grade N52) mounted on a 3D printed test bench (figure 7 insert). The field strength of 0.75 T is determined through two methods: (1) simulated using the manufacturer's online simulator (www.kjmagnetics.com/calculator.asp) with the magnetic-property specifications of the magnets and the spacing between the magnets; and (2)

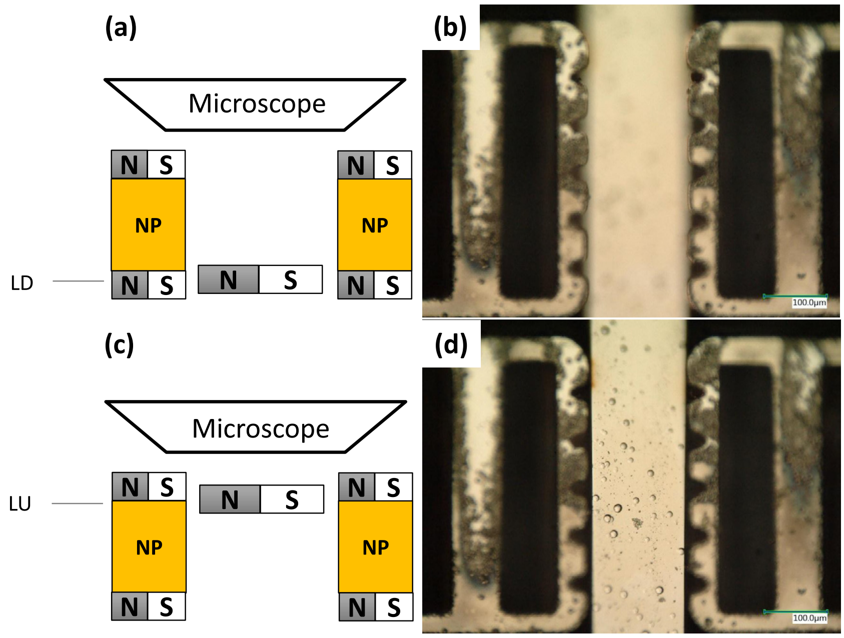

Figure 9. (a) Schematic of the latching down (LD) state (side-view) and the corresponding digital microscope image (b) (top-view), and (c) schematic of the latching up (LU) state (side-view) and the corresponding digital microscope image (d) (top-view).

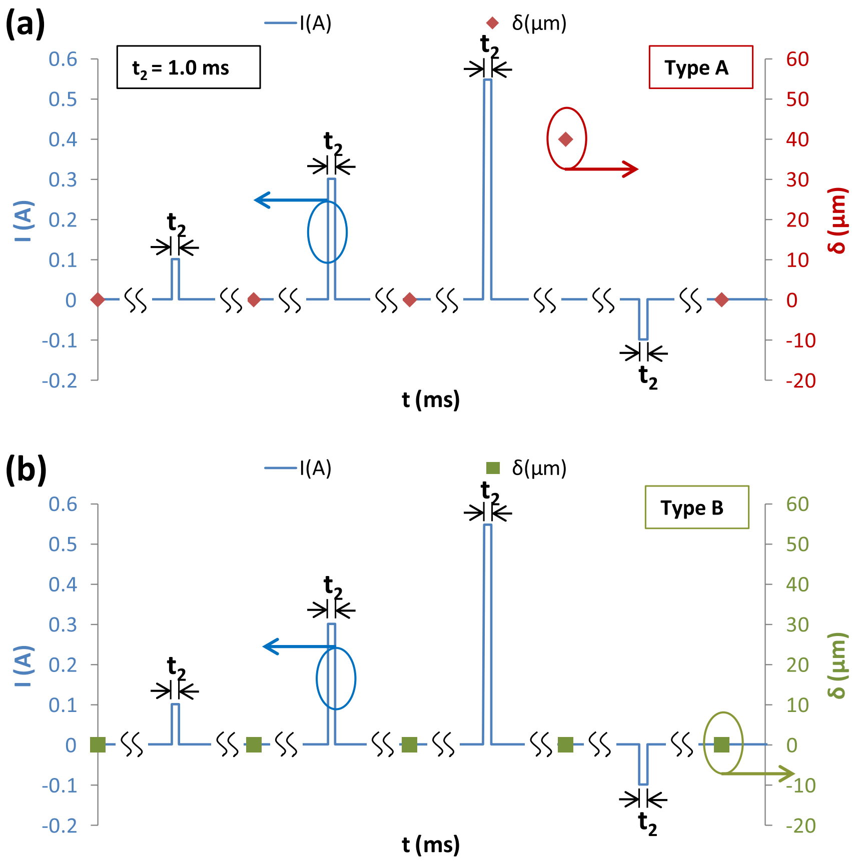

Figure 10. Static vertical displacement measured using digital microscope with a fixed pulse duration (t_2 of 1.0 ms) and various actuating current pulses (0.1, 0.3, and 0.55 A in pulse height) for (a) type A device (10 μm gap), showing an LU state 40 μm from the LD state could be triggered with a 0.55 A pulse, followed by a return of the LD state with a reverse pulse of -0.1 A. (b) Type B device (50 μm-gap), showing no LU state regardless of the pulse heights.

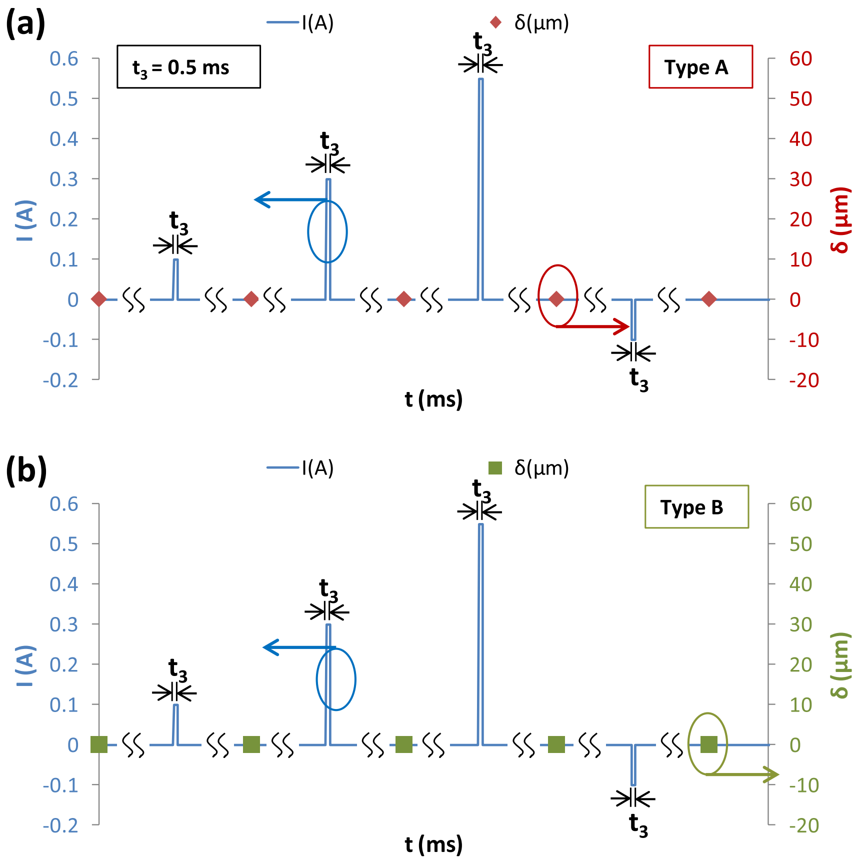

Figure 11. Static vertical displacement measured using digital microscope with a fixed pulse duration (t_3 of 0.5 ms) and various actuating current pulses (0.1, 0.3, and 0.55 A in pulse height) for (a) type A device (10 μm gap) and (b) type B device (50 μm gap). A current pulse width of 0.5 ms could not trigger LU state in either types of devices regardless of the pulse heights.

measured using a Gauss meter (Model GM2, AlphaLab, Inc.). The vertical static displacement (actuation range) at the center of the shuttle was measured by a digital microscope (Keyence VHX-5000) based on focus-detection with vertical resolution of 0.5 μm. A galvanostat (Gamry, reference 600+) was used to provide a controlled pulsed current sequence.

A series of current pulses with various pulse heights (selected pulse heights, 0.1, 0.3, and 0.55 A are plotted here for demonstration purposes) and pulse widths (10.0 ms, shown in figures 8(a) and (b); 1.0 ms, shown in figures 10(a) and (b); 0.5 ms, shown in figures 11(a) and (b)) were supplied from the galvanostat, and the before- and after-pulse vertical displacements were manually measured by the digital microscope, with the LD state (initial state) being zero displacement ($\delta = 0$ μm). Figure 8 shows the experiments with pulse width of 10.0 ms for type A (figure 8(a)) and type B (figure 8(b)) devices. The primary vertical axis records various pulse heights whereas the secondary vertical axis records the displacement. The horizontal axis records time elapsed, where even though pulse width was precisely recorded, due to the manual nature of the focus-detection based displacement measurement, the exact time at which displacement data were measured was not traceable. As can be seen from figure 8(a), the shuttle was initially at LD state, corresponding to the vertical displacement (δ) of 0 μm. A current pulse of 0.1 A in height and 10.0 ms in width was firstly applied, followed by an after-pulse displacement measurement. The zero after-pulse displacement indicates the shuttle was not switched into LU states. Sequentially increased pulse heights (same pulse width) were subsequently applied to the system followed by the after-pulse displacement measurements in a similar fashion. It was observed that for the type A device, a current pulse height as high as 0.55 A was needed in order to switch the LD state ($\delta = 0$ μm) to LU state ($\delta = 40$ μm). A minimum negative pulse of -0.1 A was needed to switch from the LU state back to the LD state. However, for the type B device shown in figure 8(b), no LU state was observed; zero displacement before and after the current pulse was recorded, even though dynamic behaviors such as vibration can be seen when pulsing occurs through the recorded video (refer to supplementary materials stacks.iop.org/JMM/28/105010/mmedia). The absence of a defined LU state in type B devices is in accordance with the discussion of section 2.3. The experimental pulsing-up current height (0.55 A) and -down current height (-0.1 A) differ from the simulated values (0.19 A and -0.05 A). The possible reasons of these differences might be traced back to (1) testing related error (e.g. misaligned magnetic field to current angle, magnetic field deviation due to test bench assembly) and (2) fabrication related error (e.g. fabrication dimension variations and etching defects such as pinholes, which might lower the mechanical stiffness of the shuttle, reducing the magnetic forces/pulse current needed to switch between stable positions).

A video clip demonstrating the operation of the bi-stable actuator (10 ms pulse on and 1 s pulse off) can be found in the supplementary material. Screen shots of the video clip can be seen in figure 9. The schematic of the LD state and the corresponding microscope image can be found in figures 9(a) and (b), respectively; the schematic of LU state and the corresponding image is shown in figures 9(c) and (d).

Similarly, experiments with a fixed pulse width of 1.0 ms for type A and type B devices are shown in figures 10(a) and (b). For the type A device, same minimum current pulse heights (pulsing-up current height (0.55 A) and pulsing-down current height (-0.1 A)) and actuation range (40 μm) has been recorded; and for type B device, no LU state was observed. An even smaller pulse width of 0.5 ms, however, could not trigger the LU state in either type of devices, shown in figures 11(a) and (b). This observed behavior may be explained by considering the shuttle as a mass-spring system, with a reduced amplitude response above the natural mechanical resonant frequency of the system (determined to be 1121.5 Hz using the MEMS module of COMSOL Multiphysics, not shown).

Utilization of a pulsed current not only reduces possible Joule heating effects, but also minimizes the required energy input (I^2Rt, where I is the pulsed current height, $R = 2\ \Omega$ is the nominal resistance of the device, t is the pulse duration). The minimal required energy input for switching from LD to LU state is 0.6 mJ, and from LU to LD is 0.02 mJ. In the latching states, due to the magnetostatic latching force, no external energy is needed to keep the shuttle in the designated latched positions.

5. Conclusion

A bi-stable vertical magnetic actuator with non-contact latching is presented. FEA was used to predict critical gap size leading to bi-stable latching behaviors. This device was fabricated utilizing two technologies developed in-house: a single-mask process for dual-height metallic structures, and a magnetic microlamination technology taking advantage of the multilayer-structure-induced spatially varying magnetic field patterns. Bi-stable latching and vertical displacement of 40 μm has been achieved in these MEMS actuators with small energy input and zero standby power consumption.

ORCID iDs

Yuan Li https://orcid.org/0000-0002-4313-8224

References

[1] Sutanto J, Hesketh P J and Berthelot Y H 2006 Design, microfabrication and testing of a CMOS compatible bistable electromagnetic microvalve with latching/unlatching mechanism on a single wafer *J. Micromech. Microeng.* **16** 266

[2] Sarajlic E, Yamahata C, Cordero M and Fujita H 2009 An electrostatic 3-phase linear stepper motor fabricated by vertical trench isolation technology *J. Micromech. Microeng.* **19** 074001

[3] Taylor W P, Brand O and Allen M G 1998 Fully integrated magnetically actuated micromachined relays *J. Microelectromech. Syst.* **7** 181–91

[4] Glickman M, Tseng P, Harrison J, Niblock T, Goldberg I B and Judy J W 2011 High-performance lateral-actuating magnetic MEMS switch *J. Microelectromech. Syst.* **20** 842–51

[5] Niarchos D 2003 Magnetic MEMS: key issues and some applications *Sensors Actuators* A **109** 166–73

[6] Cho I-J, Song T, Baek S-H and Yoon E 2005 A low-voltage and low-power RF MEMS series and shunt switches actuated by combination of electromagnetic and electrostatic forces *IEEE Trans. Microw. Theory Tech.* **53** 2450–7

[7] Wang N and Arnold D P 2010 Batch-fabricated electrodynamic microactuators with integrated micromagnets *IEEE Trans. Magn.* **46** 1798–801

[8] Rostaing H, Stepanek J, Cugat O, Dieppedale C and Delamare J 2005 Magnetic, out-of-plane, totaly integrated bistable/spl mu/-actuator *The 13th Int. Conf. on Solid-State Sensors, Actuators and Microsystems, 2005. Digest of Technical Papers. TRANSDUCERS'05* pp 1366–70

[9] Li Y, Kim M and Allen M G 2018 A single mask process for the realization of fully-isolated, dual-height MEMS metallic structures separated by narrow gaps *J. Micromech. Microeng.* **28** 027001

[10] Kim M, Kim J, Herrault F, Schafer R and Allen M G 2013 A MEMS lamination technology based on sequential multilayer electrodeposition *J. Micromech. Microeng.* **23** 095011

[11] Herrault F, Galle W, Shafer R and Allen M 2011 Electroplating-based approaches for volumetric nanomanufacturing *Proc. Technical Digest Technology for Future Micro-Nano Manufacturing* pp 71–4

[12] Li Y, Kim J, Kim M, Armutlulu A and Allen M G 2016 Thick multilayered micromachined permanent magnets with preserved magnetic properties *J. Microelectromech. Syst.* **25** 498–507

[13] Kim J *et al* 2013 Nanolaminated permalloy core for high-flux, high-frequency ultracompact power conversion *IEEE Trans. Power Electron.* **28** 4376–83

[14] Agashe J S and Arnold D P 2008 A study of scaling and geometry effects on the forces between cuboidal and cylindrical magnets using analytical force solutions *J. Phys. D: Appl. Phys.* **41** 105001

[15] Casperson L W 2002 Forces on permeable conductors in magnetic fields *Am. J. Phys.* **70** 163–8

[16] McDonald K T 2002 Magnetic force on a permeable wire

[17] Peterman M C, Huie P, Bloom D and Fishman H A 2003 Building thick photoresist structures from the bottom up *J. Micromech. Microeng.* **13** 380

[18] Walton A 2017 Integration of electrodeposited Ni–Fe in MEMS with low-temperature (Edinburgh: University of Edinburgh, School of Engineering) (https://doi.org/10.7488/ds/1985)

[19] Williams K R, Gupta K and Wasilik M 2003 Etch rates for micromachining processing-part II *J. Microelectromech. Syst.* **12** 761–78

[20] Thanu D P R, Venkataraman N, Raghavan S and Mahdavi O 2009 Dilute HF solutions for copper cleaning during BEOL processes: effect of aeration on selectivity and copper corrosion *ECS Trans.* **25** 109–16

[21] Todd G 2003 Thin film resistance to hydrofluoric acid etch with applications in monolithic microelectronic/MEMS integration *PhD Thesis* Georgia Institute of Technology